JOURNAL OF MATERIALS SCIENCE 14 (1979) 1807–1816

The effect of crystallographic orientation on damage in MgO due to spherical particle impact

D. G. RICKERBY, B. N. PRAMILA BAI, N. H. MACMILLAN
Materials Research Laboratory, The Pennsylvania State University, University Park, PA 16802, USA

A single stage gas gun has been used to fire spherical chrome steel and WC particles at variously oriented and prepared MgO single crystals at velocities of up to 350 m sec^{-1}. The resultant damage has been studied by optical and scanning electron microscopy, dislocation etching and surface profilometry, and mass losses have been determined gravimetrically. The measured crater dimensions and the mass loss data have been compared with the predictions of a simple analytical model of the impact event.

1. Introduction

The erosion of materials by solid particle impingement is a serious problem in many industrial and aerospace systems. Yet, despite a growing technical literature on the subject, only relatively few attempts have been made to understand the fundamental mechanisms involved [1, 2]. As a result, little or nothing is yet known about the effect of even such a basic parameter as crystallographic orientation on the rate of material loss. It has, however, become clear that single impact studies are a useful means of investigating this and other questions about the mechanisms of erosion [3, 4]. This is because material removal during erosion occurs as the result of a series of essentially independent impact events. Moreover, it has also been recognized that, even though erosive particles are usually random in shape, a spherical particle in many cases can provide a reasonable simulation of a typical impact event [4].

At the present level of understanding, this is ample justification for using spherical particles and taking advantage of the experimental reproducibility and theoretical tractability that derive from doing so. In particular, when the impact direction is normal to the target surface, spherical geometry allows an analytical solution to the equation of motion of the particle to be obtained. It is for these reasons that the experimental work reported herein has been restricted to single normal impacts of spherical particles against surfaces of different crystallographic orientation. MgO was chosen as the target material because: (i) it is available in the form of large monocrystals, (ii) it is cubic and therefore easily oriented, (iii) its elastic and plastic properties are well understood, (iv) its chemical polishing and dislocation etching characteristics are well established, and (v) it is relatively easy to handle without introducing extraneous damage.

2. Experimental

A 16 mm bore gas gun, developed from a design by Hutchings and Winter [5, 6], was used to fire the erosive particles at the requisite velocities. These particles were mounted on nylon sabots for firing, and were separated from them at the muzzle by means of a steel muzzle block which stopped the sabot virtually instantaneously but allowed the particle to pass on through a small hole. Sabot velocities were determined immediately before reaching the muzzle by a photoelectric time-of-flight device. These measurements were estimated to be accurate to within ± 1%, and the velocities attained at a given firing pressure were generally reproducible to better than ± 5%.

The targets were mechanically and/or chemically polished 10 mm × 10 mm monocrystalline MgO slabs about 5 mm thick. Those slabs oriented parallel to {100} were first rough-shaped by cleavage, and those parallel to {110} or {111} by cutting with a water-cooled diamond saw. Thereafter, all

0022–2461/79/081807–10 $03.00/0

slabs were successively mechanically polished on wet 240, 320, 400 and 600 grit SiC papers and Buehler Texmet* cloths loaded with aqueous slurries of 1, 0.3 and 0.05 μm Al_2O_3 particles. Some specimens then received a further chemical polish in boiling aqueous H_3PO_4 to which a small amount of concentrated H_2SO_4 or HNO_3 had been added [7, 8]. The optimum solution concentration (which determined the boiling temperature) and polishing time varied with surface orientation [9]; but in each case it was shown by successively polishing and etching (by immersion in boiling concentrated HNO_3 for 10 sec [8]) that all mechanical damage had been removed. Finally, to facilitate subsequent handling, the polished slabs were flush mounted in standard sized cylinders of Koldmount self-curing resin.† X-ray Laue diffraction studied showed that the polished and mounted target surfaces were typically within 2° of the desired crystallographic orientation.

Two types of crystal, hereinafter referred to as A and B,‡ were used in the experiments. The former were colourless, whereas the latter varied from an almost colourless to a pronouncedly yellow appearance, indicating a variable impurity content. Emission spectroscopic studies of one crystal of type A and several of type B produced the results summarized in Table I, and etch pit counts on chemically polished and etched {1 0 0} surfaces indicated that both types of crystal had initial dislocation densities $\sim 10^5\,cm^{-2}$.

Two kinds of erosive particles were employed. WC spheres weighing 30 ± 1 mg, and of nominal diameter 1.575 ± 0.025 mm and Vickers hardness number (VHN) $\sim 2000\,kg\,mm^{-2}$ [10], were fired at surfaces of all three orientations; and precision manufactured chrome steel spheres weighing 16.2 mg, having a diameter of 1.5875 mm and a sphericity§ of 0.00065 mm, and having a Rockwell C hardness of 60 to 66,¶ were used to impact {1 0 0} surfaces in order to investigate the effect of particle hardness.

The impact craters formed were examined by surface profilometry and by optical and scanning electron microscopy (SEM). The first of these instruments provided cross-sectional profiles of the craters at equidistant (50 μm) intervals, allowing the determination of crater volume by the trapezoidal rule. In addition, crater depth and diameter were determined from the profile of a diametral section, which was assumed to be the section having the largest area below the original, undisturbed surface level.

TABLE I Semi-quantitative spectrochemical analyses of MgO crystals (p.p.m.)

Element	Crystal type A	Crystal type B
Ca	200	100–200
Al	40	40–100
Mn	50	50
Fe	100	100–200
Si	50	50
Ti	50	20

Lastly, in order to determine the mass loss associated with impact damage (typically $\sim 10^{-3}$ g), each specimen was weighed before and after it was impacted. These measurements were reproducible to within $\sim \pm 5 \times 10^{-5}$ g, and this scatter was attributed to changes in the water content of the slightly hygroscopic Koldmount resin employed to mount the specimens.

3. Theoretical model of the impact

Following Tabor [11] and Andrews [13], consider a rigid sphere of radius r and mass m impacting normally on an ideal plastic–rigid half-space. At some instant during the impact the situation is as illustrated in Fig. 1, i.e. the projectile is moving

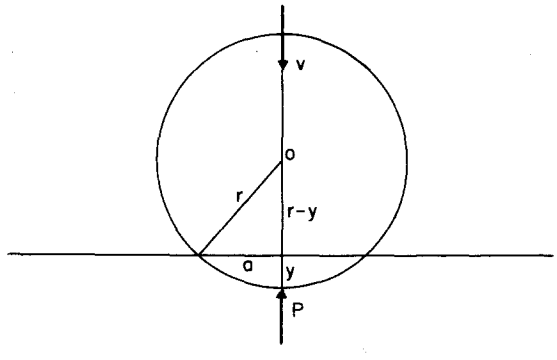

Figure 1 Schematic diagram of a spherical particle impinging normally on a half space.

* Buehler Ltd., 2120 Greenwood Street, Evanston, Illinois, USA.
† Vernon-Benshoff Co., 413 North Pearl Street, Albany 1, NY, USA.
‡ Supplied by: (A) A. Clauer, Battelle Memorial Laboratories, Columbus, OH; and (B) R. C. DeVries, General Electric Research and Development Center, Schenectady, NY, USA.
§ Difference between maximum and minimum diameters.
¶ Variously reported as equivalent to VHN's of 765 to 960 $kg\,mm^{-2}$ [11] and 700 to 860 $kg\,mm^{-2}$ [12].

with a velocity v against a resistive force P, the radius of contact is a, and the depth of penetration is y. If it is assumed that the indentation pressure, or dynamic hardness, p_d is constant throughout the impact and is independent of the particle velocity,* it follows that $P = \pi a^2 p_d$, and that the equation of motion of the particle is

$$m\ddot{y} = -\pi a^2 p_d. \tag{1}$$

The solution of this equation is

$$v^2 = v_0^2 - \frac{2\pi p_d}{m}(ry^2 - y^3/3), \tag{2}$$

where v_0 is the initial impact velocity. If the sphere comes to rest at $y = l$, this gives

$$p_d = \frac{mv_0^2}{2\pi l^2(r - l/3)}, \tag{3}$$

where l is related to the crater diameter d by

$$l = r - (r^2 - d^2/4)^{1/2}. \tag{4}$$

Equations 1 to 4 are derived on the assumption that there is neither deformation of the particle during impact nor elastic recovery of the surface afterwards, whereas either or both of these may affect the situation significantly in practice. It has been reported that elastic recovery tends to reduce l, but to have little or no effect on d [11]. If plastic deformation of the particle occurs, it can be expected to absorb energy that would otherwise be used in further deforming the target, and to thereby decrease the crater volume V, cause concomitant reductions in both d and l, and affect crater sphericity, with the result that the relation between d and l will no longer be that given in Equation 4. In either event, therefore, the measured crater depth, hereinafter designated l', may differ from the depth l implied by the theoretical model. However, only when the impacting particle deforms plastically does it seem likely that there will be any significant deviation of the crater diameter from the predicted value of d; and such a deviation can be detected by conducting parallel experiments with particles of different hardness. It is therefore assumed initially that the measured values of d are consistent with the predictions of the original model and may be used in calculating first l and then p_d. Furthermore, it is also assumed that plastic deformation of the target occurs as a radial outflow of material without any piling up above the level of the original surface. In practice, pile-up does occur, and so for consistency all measurements of crater dimensions were made relative to the original level of the undisturbed surface.

It should also be noted that, since the volume of a spherical cap of radius r and depth l is $\pi l^2(r - l/3)$, Equation 3 can be rewritten as

$$p_d V = \tfrac{1}{2}mv_0^2. \tag{5}$$

This expression, which is valid for any shape of crater when p_d is constant, is a statement of the energy balance implicit in the proposed model – namely, that all of the kinetic energy of the impacting particle is consumed in deforming the target plastically during crater formation, and that none is dissipated by plastic deformation of the particle or elastic recovery of the target. Equation 3 can also be rearranged as

$$l = \left[\frac{mv_0^2}{2\pi p_d(r - l/3)}\right]^{1/2}, \tag{6}$$

and then solved iteratively to obtain l in terms of p_d, the first iteration being

$$l \simeq \left[\frac{mv_0^2}{2\pi p_d r}\right]^{1/2}. \tag{7}$$

And similarly, Equation 4 can be rearranged as

$$d = 2(2rl - l^2)^{1/2} \tag{8}$$

to give d in terms of l.

Finally, it is useful to make an order of magnitude estimate of the plastic strain rate during an impact event. This can be done straightforwardly for the present model of an ideal plastic–rigid target struck normally by a rigid sphere, for Tabor [11] has shown that: (i) a "representative value" of the strain ϵ in the complex strain field generated in the impact zone is

$$\epsilon \simeq 0.1d/r, \tag{9}$$

and (ii) the impact duration t is independent of particle velocity and given by

$$t = \frac{\pi}{2}\left(\frac{m}{2\pi p_d r}\right)^{1/2}. \tag{10}$$

It follows that the mean strain rate $\dot{\epsilon}$ during the impact is

$$\dot{\epsilon} \simeq 0.16d\left(\frac{p_d}{rm}\right)^{1/2} \simeq 0.064\frac{dv_0}{rl} \tag{11}$$

*Note also that p_d is, in general, larger than the static hardness p_s [22].

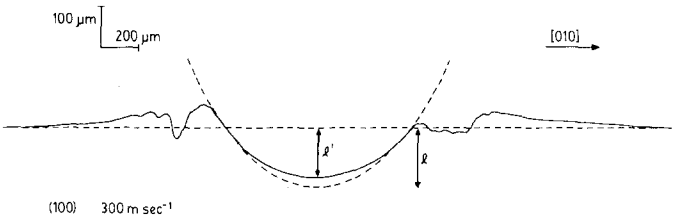

Figure 2 A diametral profile of a crater in a {100} MgO surface produced by the impact of a steel sphere. The broken lines indicate the original surface level and the outline of the sphere.

(from Equation 7). In the present work, typical values of t and $\dot{\epsilon}$ were $\sim 1\,\mu$sec and $\sim 10^5\,\text{sec}^{-1}$, respectively.

4. Results

4.1. Impacts using steel particles

Figs. 2 to 5 summarize the results obtained by firing single steel spheres at chemically polished {100} surfaces of A-type crystals at velocities of up to $\sim 350\,\text{m sec}^{-1}$.

The first of these figures shows (at a 2:1 ratio of vertical to horizontal magnification) a diametral profilometer trace through a crater created by a $300\,\text{m sec}^{-1}$ impact. Superimposed on this profile is the diametral profile of a pristine steel sphere. It is apparent that the two profiles do not correspond and, in particular, that the measured depth is less than that predicted. Profilometry and SEM studies of spent spheres revealed that this discrepancy could be attributed to flattening of the spheres by plastic deformation during impact, at least at higher impact velocities.

Figs. 3 to 5 show the variation with impact velocity of the measured crater diameter, depth and volume, respectively. The values of the dynamic hardness calculated from the individual data points in Fig. 3 by means of Equations 3 and 4 reveal no systematic variation with velocity, but are distributed about a mean value of $1450\,\text{kg mm}^{-2}$ with a standard deviation of $210\,\text{kg mm}^{-2}$. In comparison, the static VHN was measured as $875\,\text{kg mm}^{-2}$, with a standard deviation of $19\,\text{kg mm}^{-2}$. The solid line drawn through the data of Fig. 3 was calculated from the mean value of the dynamic hardness and Equations 6 to 8. The good fit of this line to the experimental data implies, however, only that the scatter in the calculated values of the dynamic hardness is random in nature and limited in extent. In contrast, although the solid lines superimposed on the data for crater depth and volume shown in Figs. 4 and 5 also were obtained from this same value of the dynamic hardness (by means of Equations 6 and 7 in the case of Fig. 4, and Equation 5 in the case of Fig. 5), it is seen that the experimental points systematically diverge from both lines as the impact velocity increases. In

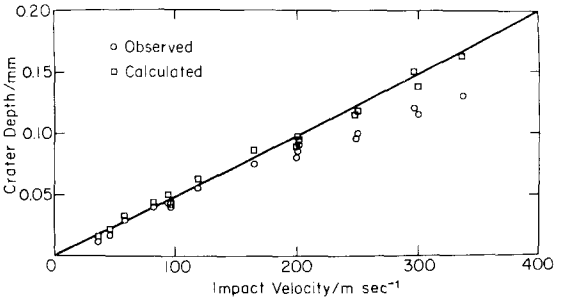

Figure 4 Depths of craters produced by the impact of steel spheres on {100} surfaces.

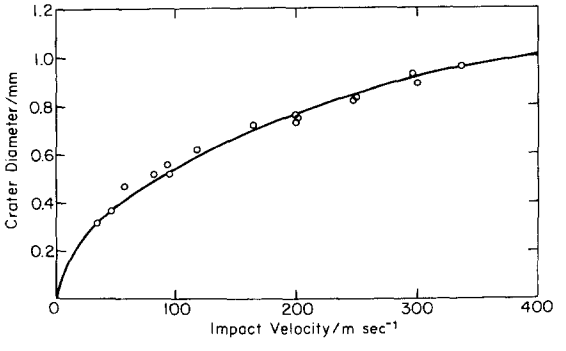

Figure 3 Diameters of craters produced by the impact of steel spheres on {100} surfaces.

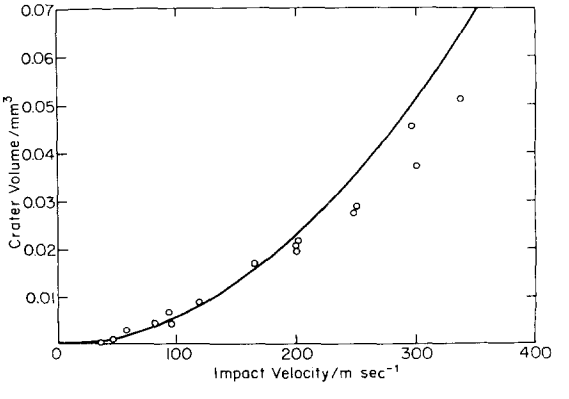

Figure 5 Volumes of craters produced by the impact of steel spheres on {100} surfaces.

the case of Fig. 4 this trend is confirmed by comparison of the experimental data with the points calculated from the measured crater diameters by means of Equation 4.

4.2. Impacts using WC particles

This section presents the results of a similar series of experiments in which single WC spheres were fired at variously polished {100}, {110} and {111} surfaces of B-type crystals, again using velocities of up to 350 m sec^{-1}. These spheres exhibited negligible plastic deformation during impact.

Figs. 6a to c show scanning electron micrographs of three craters resulting from impacts against chemically polished {100}, {110} and {111} surfaces. It is clear from the very different patterns of {100} and {110} cleavage cracks and {110} slip traces surrounding these three craters that the mode of material removal due to impact is markedly sensitive to crystallographic orientation. On a {100} surface, as noted by Hooker and Adler [14], a roughly square eroded region is formed around a central plastic crater by intersection of {100} and {110} cleavage cracks. This region is deepest along its ⟨110⟩ diagonals, and the crater rim is most extensively chipped away in these directions also. In the {110} case, the first material lost is that broken out along the ⟨111⟩ directions in the impact surface by intersection of {110} cleavage cracks. At higher impact velocities this

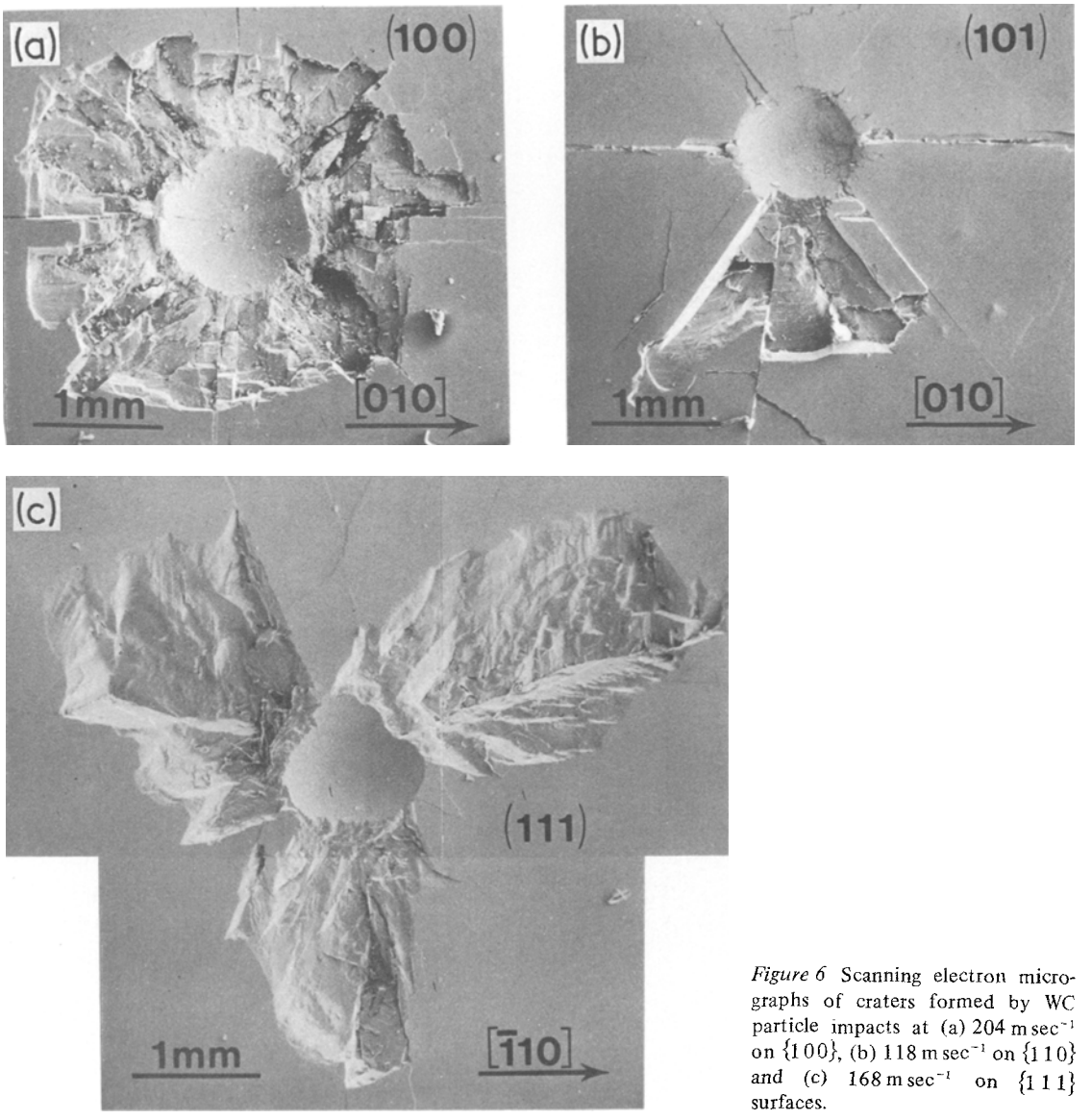

Figure 6 Scanning electron micrographs of craters formed by WC particle impacts at (a) 204 m sec^{-1} on {100}, (b) 118 m sec^{-1} on {110} and (c) 168 m sec^{-1} on {111} surfaces.

process is augmented by chipping due to intersection of these same cracks either with subsurface {1 1 0} cracks lying parallel to the impact surface and/or with {1 0 0} cleavage cracks lying at 45° to it. There is also a tendency in this orientation for long thin triangular prism-shaped fragments to be broken out along the ⟨1 0 0⟩ direction in the impact surface by intersection of two {1 0 0} cracks with this surface. The damage arising from impact against a {1 1 1} surface exhibits strongly the three-fold symmetry of this surface, with material loss occurring primarily by {1 0 0} cleavage from three petal-shaped areas ("wings") that extend along ⟨2 1 1⟩ directions. Fig. 7, which shows a crater formed at a lower impact velocity, reveals that the material in these wings is not detached when this velocity is small, but is merely raised above the original surface. Detachment begins only when the impact velocity exceeds ~ 100 m sec^{-1}, and occurs over an ever increasing area as this velocity increases, with the wings coalescing to form a continuous eroded region completely surrounding the central plastic crater at velocities around 200 to 300 m sec^{-1}. In this velocity regime the damage bears some superficial resemblance to that occurring in polycrystalline ceramics [15], although the detailed fracture processes involved in the two cases are rather different.

Profilometer traces through diametral sections of craters in chemically polished specimens of the same three orientations are shown in Figs. 8a to c at a 2:1 ratio of vertical to horizontal magnification. These traces were obtained by traversing the profilometer stylus across the impact regions in the particular crystallographic directions noted in the figures*. Several features of these traces are worthy of note. First, each exhibits a central plastic crater that is complete and can be measured accurately. This feature is usually lost at higher impact velocities due to encroachment of the surrounding eroded region into the central crater. Second, below the level of the original surface, each trace is (i) symmetrical and (ii) of the same curvature as the WC sphere that created it. Moreover, traces of other diametral sections obtained by traversing the impact zone in different crystallographic directions reveal the same features. It follows that both plastic deformation of the WC particle and elastic recovery of the target in the central crater region are negligible, and this implies that the difference between the measured and the predicted crater depths observed when steel particles were used can be attributed almost entirely to plastic deformation of these particles during the impact event. A third significant feature of the various diametral traces obtained from different directions of traverse is that most are not symmetrical above the level of the undisturbed surface. This asymmetry, which can be seen in Fig. 8c, for example, arises from material in the vicinity of the crater rim piling up by slip on the active slip planes in the active slip directions. The resultant crater rims exhibit four-, three- and two-fold symmetries in the cases of {1 0 0}, {1 1 1} and {1 1 0} target surfaces, respectively.

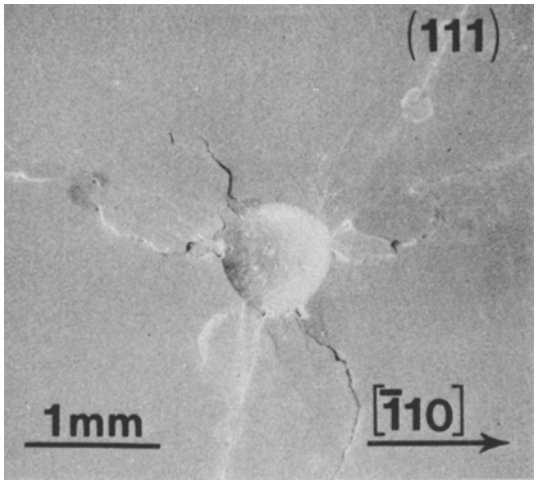

Figure 7 Scanning electron micrograph of a crater formed by the impact of a WC particle at 89 m sec^{-1} on a {1 1 1} surface.

Figs. 9 and 10 show the variation with impact velocity of the measured crater diameter and depth, respectively, for impacts on chemically polished {1 0 0} surfaces. The mean value of the dynamic hardness was first calculated from the individual data points in Fig. 9 and then used to obtain the theoretical lines shown in the figures exactly as in the previous section. The important point to note is that, while there is random scatter in the individual data points in Fig. 10, there is no systematic deviation from the theoretical line of the sort seen when steel particles are used. The corresponding crater volumes are shown in Fig. 11, together with those measured on chemically polished {1 1 0} and {1 1 1} surfaces.

Mass loss data for the same series of impacts are plotted in Fig. 12, and superimposed on these data

*Quantitative measurements of crater dimensions were always made in these same directions.

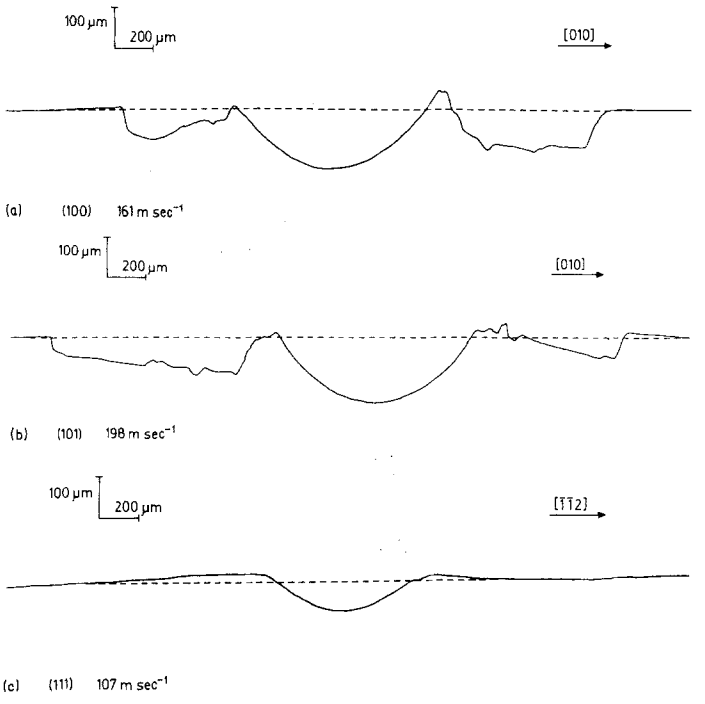

Figure 8 A comparison between diametral traces through impact craters made by WC particles in MgO surfaces of different orientations.

by the least-squares method are parabolas of the form

$$m_1 = kmv_0^2, \qquad (12)$$

where m_1 is the mass loss and k is a constant dependent on the crystallographic orientation of the target. The good fit suggests that it is not unreasonable to suppose that, for a single impact, the mass loss depends on the kinetic energy of the impacting particle. It will be noted that, in comparison with {100} surfaces impacted at the same velocity, {110} surfaces yield a comparable crater volume and ~3 times the mass loss, while {111} surfaces give rise to a crater of about half the volume and about double the mass loss.

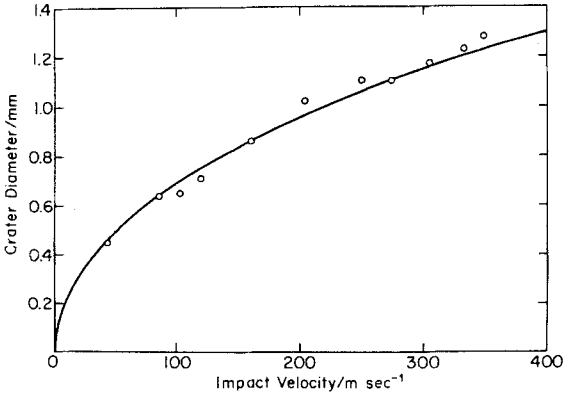

Figure 9 Diameters of craters due to impacts by WC spheres on chemically polished {100} surfaces.

In order to examine the influence of target surface condition on the impact event, further experiments using WC particles were carried out on {100} and {110} surfaces that had been given only

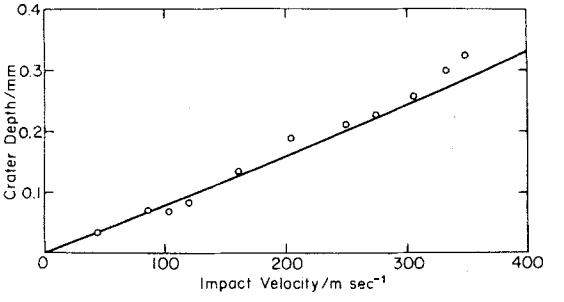

Figure 10 Depths of craters due to impacts by WC spheres on chemically polished {100} surfaces.

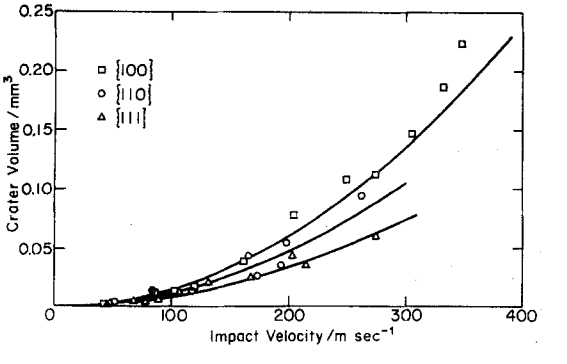

Figure 11 Volumes of craters due to impacts by WC spheres on chemically polished MgO surfaces.

TABLE II Summary of the results of impact experiments with WC particles.

Surface orientation	Polish	p_d(kg mm^{-2})*	p_s(kg mm^{-2})*		$k \times 10^6$(m^{-2}sec^2)
			(M_v)	(M_B)	
{100}	chemical	1030 ± 180	995 ± 24	185 ± 23	2.02
{100}	mechanical	1170 ± 240	1013 ± 28	213 ± 47	3.71
{110}	chemical	1310 ± 310	972 ± 29	236 ± 34	5.80
{110}	mechanical	1090 ± 240	1014 ± 30	223 ± 75	7.18
{111}	chemical	1860 ± 470	999 ± 20	329 ± 59	3.96

* The figures given are mean values ± one standard deviation.

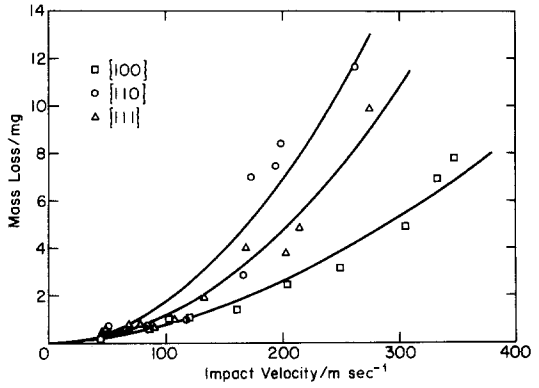

Figure 12 Mass loss data for impacts by WC spheres on chemically polished MgO surfaces.

the mechanical polish. The results indicated that this inferior finish exerted little influence on the size of the central plastic crater formed, but caused a significant increase in the mass loss.

The results of all five sets of dynamic hardness and mass loss measurements made using WC particles are summarized in Table II, together with corresponding values of the static Meyer–Vickers hardness M_v and Meyer ball hardness M_B [16]. The Meyer–Vickers hardness was measured using a conventional Vickers diamond pyramid indenter and a load of 300 g, but calculated as the load divided by the projected rather than the actual area of contact, and is thus related to the VHN by

$$M_v = \text{VHN}/0.927. \quad (13)$$

In a similar manner, the Meyer ball hardness was determined from the ratio of the load to the projected area of contact when one of the WC spheres used in the impact experiment was pressed quasi-statically into the target surface with a load of 50 kg (which gave an indentation comparable in size to a crater formed at an impact velocity ~ 100 m sec^{-1}). These particular indicators of static hardness were selected because the dynamic hardness was also calculated on the basis of the projected rather than the actual area of contact.

It is clear from Table II that the dynamic hardness and the Meyer ball hardness both have an essentially similar dependence on (i) surface finish and (ii) surface orientation. Specifically, neither parameter is significantly affected by surface finish, and both are substantially larger for {111} surfaces than for {100} surfaces. In contrast, the Meyer–Vickers hardness is not significantly affected by either surface finish or surface orientation. But the more significant conclusion from Table II is that there is no simple correlation between the mass loss coefficient and any hardness parameter.

5. Discussion

In a semi-brittle crystal such as MgO there is a complex interaction between flow and fracture. Dislocation glide at once promotes fracture by nucleating cracks at blocked slip bands and retards it by relaxing the applied stresses, thereby reducing the forces available to propagate these cracks. Glide may also cause crack tip blunting. This complexity is clearly apparent in the confusing arrays of cracks and slip bands revealed, as in Fig. 13, by etching a crystal after impact. Nevertheless, certain features of the results presented in the preceding section can be explained in terms of the established flow and fracture properties of MgO.

To begin with, it seems clear that the relatively greater anisotropy of the dynamic and Meyer ball hardnesses as compared to the Meyer–Vickers hardness stems simply from the difference in indenter geometry. In particular, because dislocations in MgO glide on {110} planes and have ⟨110⟩ Burgers vectors, they have no tendency to move as a result of uniaxial stresses directed along ⟨111⟩ directions, but are readily activated by such stresses acting parallel to ⟨100⟩ or ⟨110⟩. Hence, "blunt" spherical indenters, which in the early

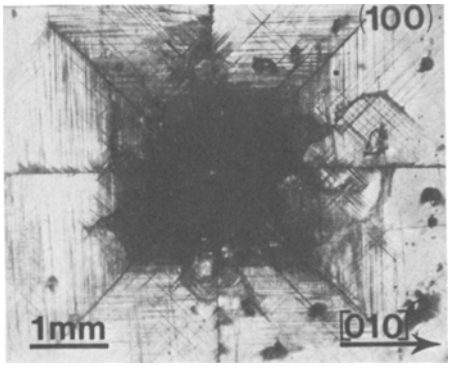

Figure 13 An impact crater on a {1 0 0} surface. The surface has been etched to reveal dislocation arrays.

stages of contact exert relatively larger compressive stresses and smaller shear stresses than a "sharper" pyramidal indenter, may be expected to give rise to a pronounced hardness maximum on {1 1 1}, as is in fact observed.

Secondly, it is possible to explain semi-quantitatively the difference between the dynamic hardness at a strain rate $\sim 10^5 \text{sec}^{-1}$ and the Meyer ball hardness at a strain rate $\sim 10^{-3} \text{sec}^{-1}$ in terms of the known dislocation stress–velocity relationship for MgO [17]. Specifically, because strain rate is proportional to dislocation velocity at constant (mobile) dislocation density (i.e., when the strain, the indenter geometry and the slip geometry are held constant) [18], the ratio p_d/M_B of these hardnesses should be equal to the stress multiplication factor required to speed up dislocation motion by a factor $\sim 10^8 \times$. Linear extrapolation of the data of Singh and Coble [17] gives a limiting value for this factor of 6 to 7 for both edge and screw dislocations, in reasonable agreement with the values of 5 to 6 for p_d/M_B reported in Table II. It is also interesting to note that dividing the longest dimension of the dislocation array seen in Fig. 13 by the impact duration time as given by Equation 10 suggests that dislocations may reach velocities as high as $2.5 \times 10^3 \text{m sec}^{-1}$ during a typical impact. This is about half the {1 1 0}⟨1 1 0⟩ shear wave velocity, and thus about half the maximum theoretical dislocation velocity.

The lack of any simple correlation between either static or dynamic hardness and mass loss is of practical interest because it demonstrates the futility of trying to relate erosion resistance to a single mechanical property. The reason for this lack is, of course, the complexity of the interrelated flow and fracture processes occurring more or less simultaneously in the impact zone during the impact event. Thus, although the flow processes that absorb most of the impact energy undoubtedly begin, and for the most part take place, beneath the impacting particles, fracture propagation is prevented by the large compressive stresses present in this region. As a result, there is produced instead a well-defined central plastic crater, the size of which defines the hardness; and cracks nucleate only at points around the crater where the hoop stress below the target surface changes from compressive to tensile. Mass loss, in contrast, is determined by the orientation dependent interaction of these cracks with one another and with the free surface as they propagate outwards from the central crater, and is thus difficult to relate to the hardness. Nevertheless, the fact that both crater volume and mass loss appear to be proportional to the kinetic energy indicates that there is some relationship between these quantities. Presumably this relationship is an expression of the frequency and the nature of the dislocation interactions leading to fracture initiation at the edge of the central plastic crater, and is obscured by the complex dependence of this process on slip line length, slip line spacing, dislocation density, and a host of other parameters.

In conclusion, it is cautioned that neither the value of the mass loss coefficients, k, listed in Table II nor the velocity exponent of two used in Equation 12 should be expected to carry over to the multiple impact situation in which the further complication of interaction of cracks from adjacent impacts arises.

Acknowledgements

Work supported jointly by the National Science Foundation under Grant No. DMR-76-02733 and the U.S. Army Research Office under Grant No. DAAG29-77-G-0100.

References

1. C. M. PREECE and N. H. MACMILLAN, *Ann. Rev. Mat. Sci.* 7 (1977) 95.
2. I. FINNIE, *Wear* **19** (1972) 81.
3. I. M. HUTCHINGS and R. E. WINTER, *J. Phys. D: Appl. Phys.* 8 (1975) 8.
4. I. M. HUTCHINGS, R. E. WINTER and J. E. FIELD, *Proc. Roy. Soc. Lond.* **A348** (1976) 379.
5. I. M. HUTCHINGS, Ph.D. Dissertation, University of Cambridge (1974).
6. I. M. HUTCHINGS and R. E. WINTER, *J. Phys. E: Sci. Instrum.* 8 (1975) 84.

7. R. J. STOKES, T. L. JOHNSTON and C. H. LI, *Trans. AIME* **215** (1959) 437.
8. G. W. GROVES, Ph.D. Dissertation, University of Cambridge (1962).
9. B. N. PRAMILA BAI and N. H. MACMILLAN, *J. Mater. Sci.* **14** (1979) 494.
10. E. K. STORMS, "The Refractory Carbides" (Academic Press, New York, 1967).
11. D. TABOR, "The Hardness of Metals" (Oxford University Press, London, 1951).
12. "Standard Hardness Conversion Tables for Metals", ASTM Standard No. E140-72.
13. J. P. ANDREWS, *Phil. Mag.* 9 (1930) 593.
14. S. V. HOOKER and W. F. ADLER, "Fracture Mechanics of Ceramics", Vol. 3, edited by R. C. Bradt, *et al.* (Plenum Press, New York, 1978).
15. A. G. EVANS, M. E. GULDEN and M. ROSENBLATT, *Proc. Roy. Soc. Lond.* **A361** (1978) 343.
16. F. A. McCLINTOCK and A. S. ARGON, "The Mechanical Behavior of Metals" (Addison-Wesley, Reading, Mass., 1966) Ch. 13.
17. R. N. SINGH and R. L. COBLE, *J. Appl. Phys.* **45** (1974) 990.
18. A. H. COTTRELL, "Dislocations and Plastic Flow in Crystals" (Oxford University Press, London, 1953).

Received 19 July 1978 and accepted 5 January 1979.